

# Amorphous Vanadium Oxide Matrixes Supporting Hierarchical Porous Fe<sub>3</sub>O<sub>4</sub>/Graphene Nanowires as a High-Rate Lithium Storage Anode

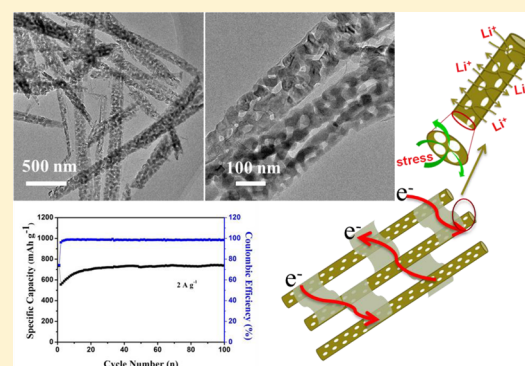
Qinyou An,<sup>§</sup> Fan Lv,<sup>§</sup> Qiuqi Liu,<sup>§</sup> Chunhua Han,<sup>\*</sup> Kangning Zhao, Jinzhi Sheng, Qiulong Wei, Mengyu Yan, and Liqiang Mai<sup>\*</sup>

State Key Laboratory of Advanced Technology for Materials Synthesis and Processing, WUT-Harvard Joint Nano Key Laboratory, Wuhan University of Technology, Wuhan 430070, China

## Supporting Information

**ABSTRACT:** Developing electrode materials with both high energy and power densities holds the key for satisfying the urgent demand of energy storage worldwide. In order to realize the fast and efficient transport of ions/electrons and the stable structure during the charge/discharge process, hierarchical porous Fe<sub>3</sub>O<sub>4</sub>/graphene nanowires supported by amorphous vanadium oxide matrixes have been rationally synthesized through a facile phase separation process. The porous structure is directly in situ constructed from the FeVO<sub>4</sub>·1.1H<sub>2</sub>O@graphene nanowires along with the crystallization of Fe<sub>3</sub>O<sub>4</sub> and the amorphization of vanadium oxide without using any hard templates. The hierarchical porous Fe<sub>3</sub>O<sub>4</sub>/VO<sub>x</sub>/graphene nanowires exhibit a high Coulombic efficiency and outstanding reversible specific capacity (1146 mAh g<sup>-1</sup>). Even at the high current density of 5 A g<sup>-1</sup>, the porous nanowires maintain a reversible capacity of ~500 mAh g<sup>-1</sup>. Moreover, the amorphization and conversion reactions between Fe and Fe<sub>3</sub>O<sub>4</sub> of the hierarchical porous Fe<sub>3</sub>O<sub>4</sub>/VO<sub>x</sub>/graphene nanowires were also investigated by in situ X-ray diffraction and X-ray photoelectron spectroscopy. Our work demonstrates that the amorphous vanadium oxides matrixes supporting hierarchical porous Fe<sub>3</sub>O<sub>4</sub>/graphene nanowires are one of the most attractive anodes in energy storage applications.

**KEYWORDS:** Iron oxides, vanadium oxides, graphene, hierarchical porous nanowires, lithium ion battery



In the past decades, concerns over environmental pollution and depletion of fossil fuels have galvanized the endeavors to develop alternative energy conversion/storage systems with high energy and power densities.<sup>1,2</sup> Among those different energy conversion/storage systems in operation or under study, lithium ion batteries (LIBs) are attracting special attention because of their high energy density and long lifespan.<sup>3–5</sup> Presently, as the commercial LIBs anode material, graphite has a relatively low theoretical discharge capacity of 372 mAh g<sup>-1</sup>. Therefore, the exploitation of different anode materials with high capacity such as alloys, metal oxides, and metal sulfides, is urgent.<sup>3</sup> Among the high-capacity anode materials, iron oxides have attracted much attention and been studied widely due to their low cost, earth abundance and ease of synthesis.<sup>6–10</sup> Nevertheless, these materials often suffer from low Li<sup>+</sup> diffusion coefficient, poor capacity retention and large volume change during Li<sup>+</sup> insertion/extraction, thus limiting their capability as substitutions for graphite as LIBs anodes.<sup>11–13</sup>

The rational design and synthesis of nanowires have been demonstrated for a variety of energy applications. For LIBs, the nanowires provide efficient ion diffusion as well as continuous electron transport pathway, which have demonstrated the superiority in lithium storage applications.<sup>14–18</sup> However, it still

remains challenging to date how to prevent the pulverization of the nanowires during the Li<sup>+</sup> insertion/extraction.<sup>19,20</sup> Porous structure can not only increase the contact area between electrode and electrolyte, which effectively facilitates the ion diffusion kinetics,<sup>21–24</sup> but also provides more space for the volume change during charge/discharge process, improving their cycle performance.<sup>25–27</sup> Therefore, creating pores in nanowire materials is one of the most effective strategies to improve the electrochemical performance.<sup>4,28–30</sup> In addition, the lithium storage process involves both ion diffusion and electron transport in the electrode materials. In order to further achieve high-rate capability, the electric conductivity needs to be enhanced. Because graphene exhibits superior electric conductivity, various hybrid nanomaterials of the graphene and active materials have been fabricated and used as electrode for LIBs recently.<sup>31–33</sup> Moreover, the graphene layers are favorable to stabilize the original structure, because it can provide mechanical flexibility for the iron oxide to accommodate volume change during cycling.<sup>34</sup>

Received: July 8, 2014

Revised: September 9, 2014

Published: October 14, 2014

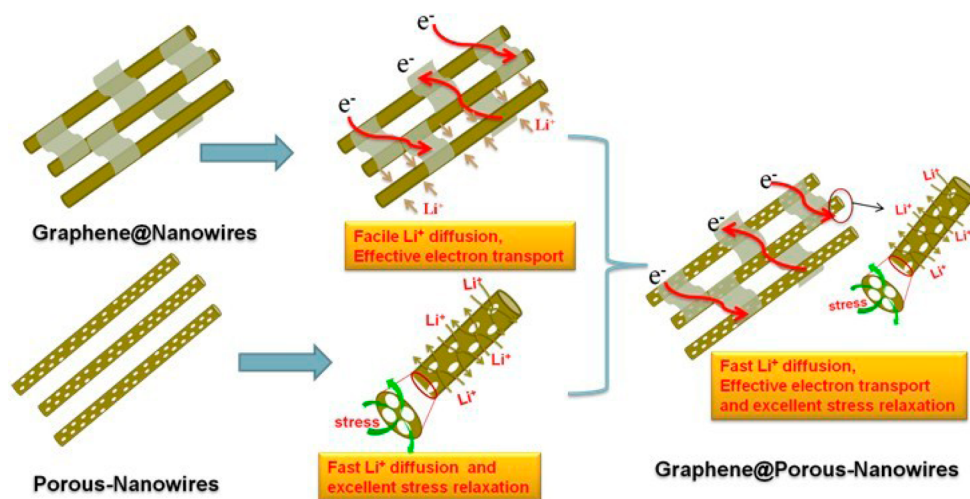


**Figure 1.** Schematic illustration of the porous nanowire composites with fast  $\text{Li}^+$  diffusion, effective electron transport, and excellent stress relaxation during  $\text{Li}^+$  extraction/insertion.

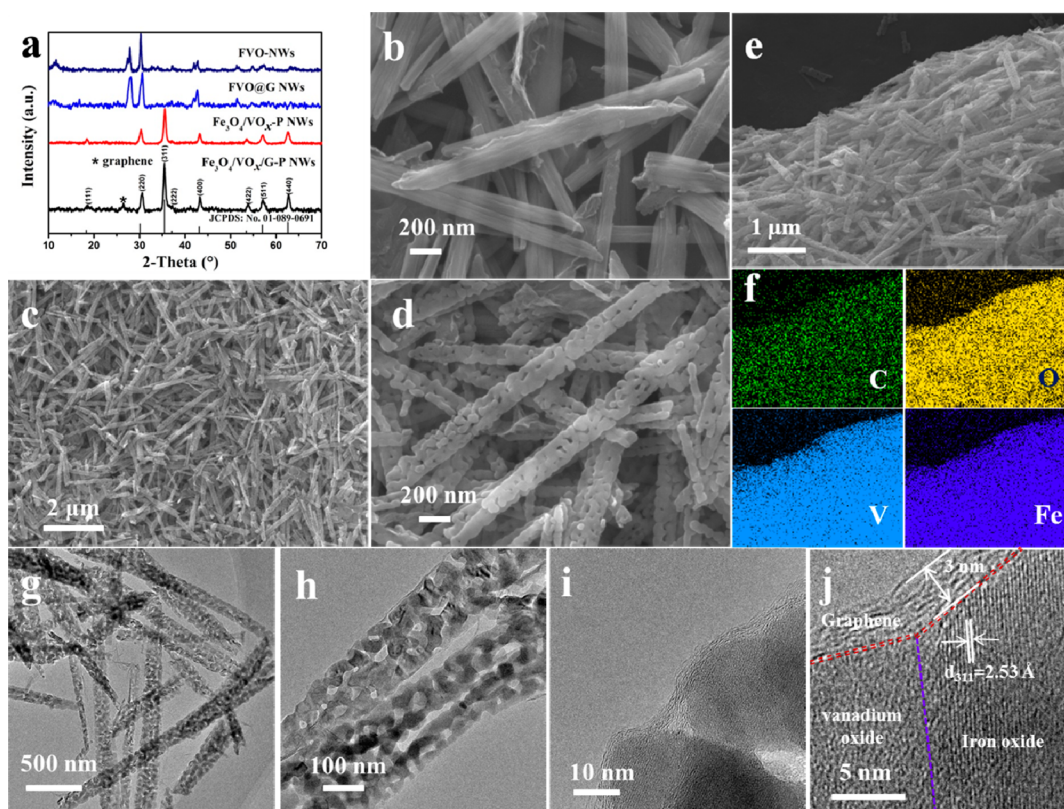


**Figure 2.** (a) XRD patterns of the FVO-NWs, FVO@G NWs,  $\text{Fe}_3\text{O}_4/\text{VO}_x$ -P NWs, and  $\text{Fe}_3\text{O}_4/\text{VO}_x/\text{G-P}$  NWs; (b) SEM image of FVO@G NWs; SEM images (c,d), EDS element mappings (e,f), TEM (g,h) and HRTEM (i,j) images of  $\text{Fe}_3\text{O}_4/\text{VO}_x/\text{G-P}$  NWs.

In the present work, we report amorphous vanadium oxides matrixes supporting hierarchical porous  $\text{Fe}_3\text{O}_4/\text{graphene}$  nanowires ( $\text{Fe}_3\text{O}_4/\text{VO}_x/\text{G-P}$  NWs) prepared by a template free hydrothermal method and subsequent heat treatment in reducing atmosphere.<sup>35</sup> The measurements of  $\text{Fe}_3\text{O}_4/\text{VO}_x/\text{G-P}$  NWs as LIB anodes are carried out. The corresponding results show that the as-synthesized products have manifested the merits of an ideal electrode material: high capacity ( $1146 \text{ mAh g}^{-1}$ ), fantastic rate capability ( $5 \text{ A g}^{-1}$ ), and cycling stability. The excellent electrochemical performance can be attributed to the unique porous hybrid nanowire architecture.

As illustrated in Figure 1, constructing the  $\text{Fe}_3\text{O}_4/\text{VO}_x/\text{G-P}$  NWs can provide not only fast  $\text{Li}^+$  diffusion and effective electron transport but also excellent stress relaxation, resulting in the excellent lithium storage performance.

Initially, in order to confirm the phase transition of iron vanadate after annealing treatment in  $\text{H}_2/\text{Ar}$  atmosphere, the crystal structures of the four representative samples were determined by X-ray diffraction (XRD) (Figure 2a). Before annealing, all diffraction peaks of the iron vanadate (FVO) and graphene decorated iron vanadate (FVO@G) can be assigned to  $\text{FeVO}_4 \cdot 1.1\text{H}_2\text{O}$ .<sup>36</sup> After annealing, the peaks of the as-

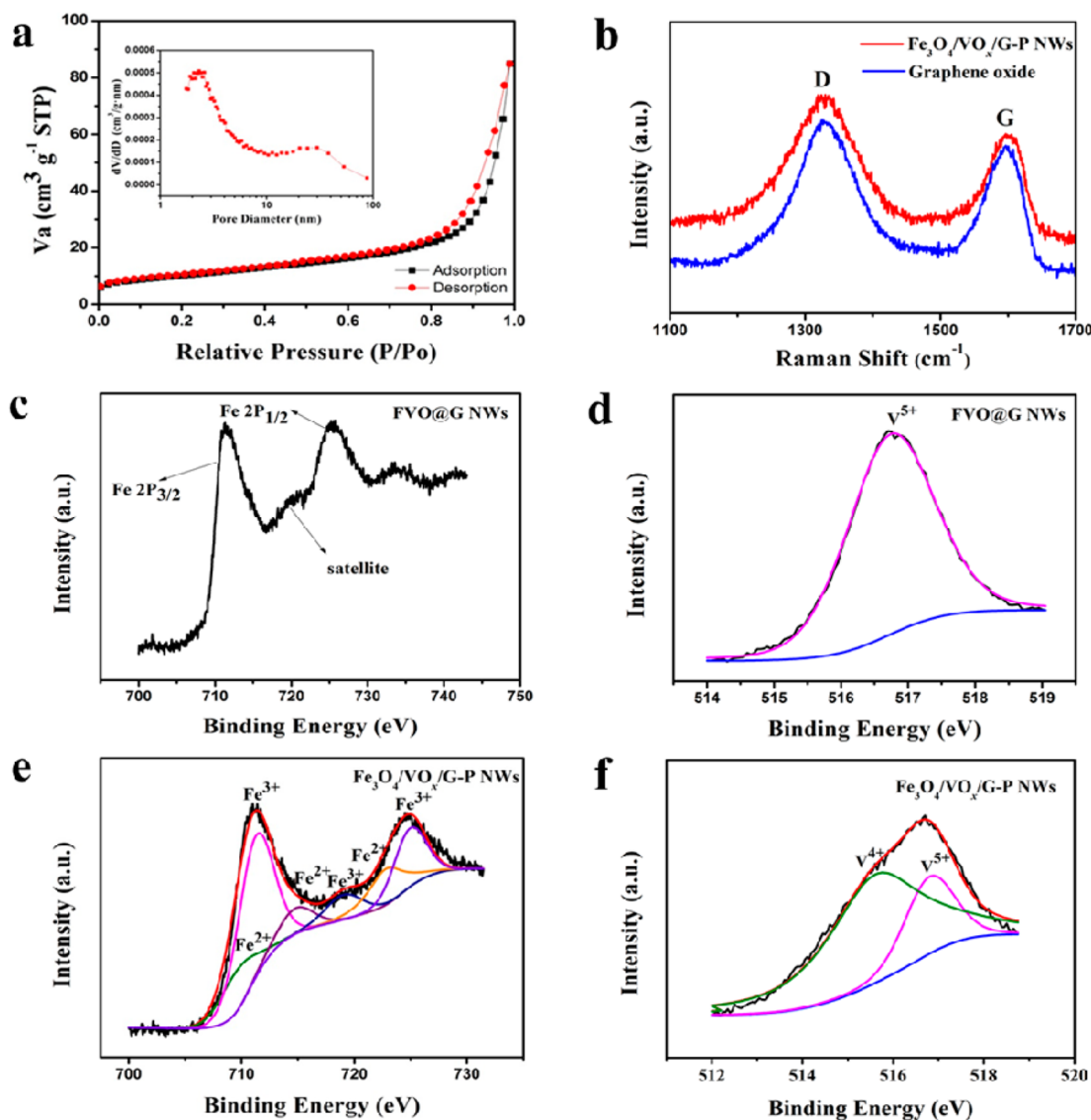


**Figure 3.** (a) Nitrogen adsorption–desorption isotherms of  $\text{Fe}_3\text{O}_4/\text{VO}_x/\text{G-P NWs}$  and corresponding pore size distribution (inset); (b) Raman spectra of the graphene oxide and  $\text{Fe}_3\text{O}_4/\text{VO}_x/\text{G-P NWs}$ ; Fe 2p XPS spectra of FVO@G NWs (c) and  $\text{Fe}_3\text{O}_4/\text{VO}_x/\text{G-P NWs}$  (e); V 2p XPS spectra of FVO@G NWs (d) and  $\text{Fe}_3\text{O}_4/\text{VO}_x/\text{G-P NWs}$  (f).

prepared amorphous vanadium oxides matrixes supporting hierarchical porous  $\text{Fe}_3\text{O}_4$  nanowires ( $\text{Fe}_3\text{O}_4/\text{VO}_x/\text{P NWs}$ ) and  $\text{Fe}_3\text{O}_4/\text{VO}_x/\text{G-P NWs}$  can be assigned to  $\text{Fe}_3\text{O}_4$  in a  $Fd\bar{3}m$  space group (cubic unit cell) with  $a = 8.384 \text{ \AA}$  (JCPDS: No. 01-089-0691), except the diffraction peak appears at  $26^\circ$  (which is originated from graphene layers, indicating the existence of graphene<sup>37</sup>) in the pattern of  $\text{Fe}_3\text{O}_4/\text{VO}_x/\text{G-P NWs}$ . No peaks of any vanadium oxides can be observed. However, the inductive coupled high frequency plasma (ICP) result reveals that the ratio of molarity of Fe and V is about 0.94:1 (Supporting Information Table S1), which proves the existence of amorphous vanadium oxide.

The morphology and detailed structures of the as-prepared products are further investigated by scanning electron microscopy (SEM) and transmission electron microscopy (TEM). Before annealing treatment, SEM images of FVO@G NWs shown in Figure 2b and Supporting Information Figure S1 that uniform one-dimensional (1D) nanowires with about 100 nm in diameter and 2  $\mu\text{m}$  in length are observed. After annealing, the morphology is essentially preserved during the

annealing process.  $\text{Fe}_3\text{O}_4/\text{VO}_x/\text{G-P NWs}$  display a similar appearance to the pristine sample FVO@G NWs (Figure 2c). However, the highly magnified SEM image (Figure 2d) reveals that the porous structure can be observed on the surface of  $\text{Fe}_3\text{O}_4/\text{VO}_x/\text{G-P NWs}$ . The similar phenomenon can be observed between FVO-NWs and  $\text{Fe}_3\text{O}_4/\text{VO}_x/\text{P NWs}$  (Supporting Information Figure S2). The elemental mapping images (Figure 2e,f) confirm the uniform distribution of Fe, V, O, and C. To further confirm the inner architecture and the crystallographic structure of the  $\text{Fe}_3\text{O}_4/\text{VO}_x/\text{G-P NWs}$ , TEM and the high-resolution TEM (HRTEM) were carried out. TEM images indicate that the  $\text{Fe}_3\text{O}_4/\text{VO}_x/\text{G-P NWs}$  are highly porous (Figure 2g,h), while FVO@G NWs are solid (Supporting Information Figure S3). HRTEM images of  $\text{Fe}_3\text{O}_4/\text{VO}_x/\text{G-P NWs}$  display that several graphene layers of about 3 nm are at the edge of the FVO nanowire (Figure 2i,j). A lattice fringe with  $d$ -spacing of about 0.253 nm corresponds to the (311) planes of  $\text{Fe}_3\text{O}_4$  crystal. Moreover, amorphous vanadium oxide can be also observed clearly in the HRTEM image (Figure 2j), and the FFT patterns (Supporting

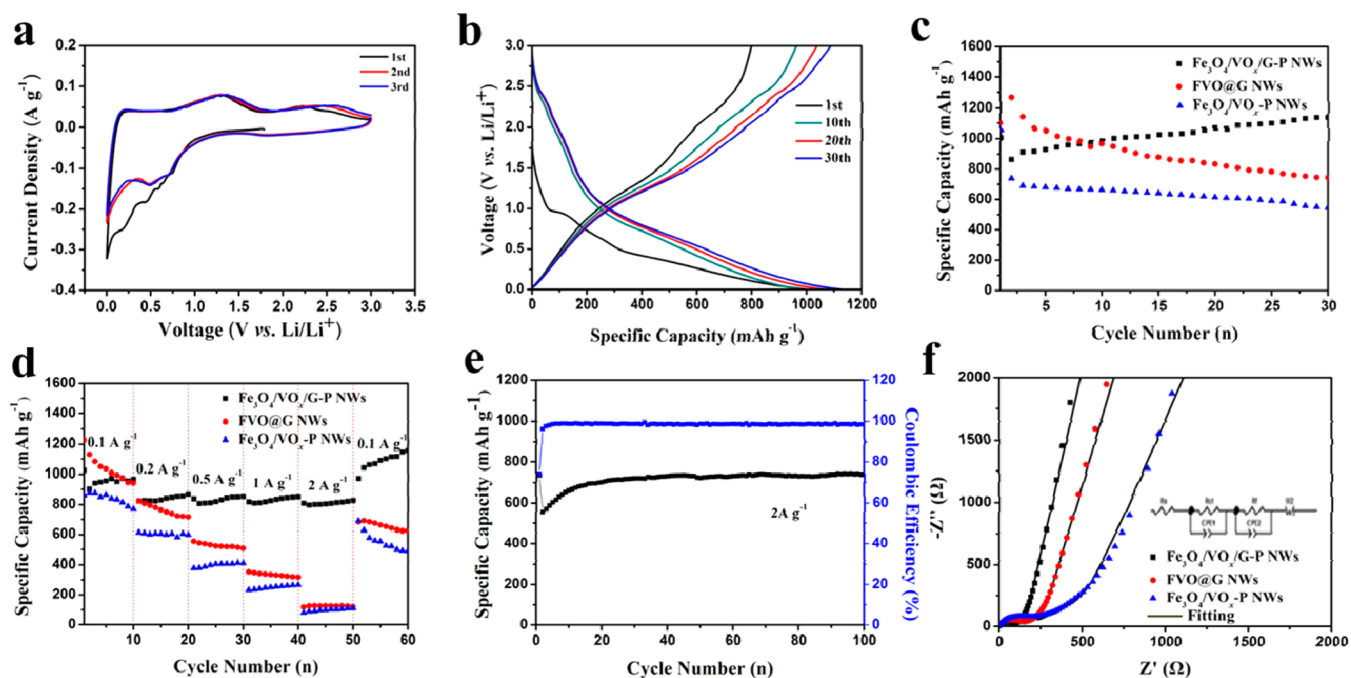


**Figure 4.** Electrochemical characteristics: (a) CV curves of  $\text{Fe}_3\text{O}_4/\text{VO}_x/\text{G-P}$  NWs at a sweep rate of  $0.1 \text{ mV/s}$  in the potential range from  $0$  to  $3.0 \text{ V}$  versus  $\text{Li}/\text{Li}^+$ ; (b) galvanostatic charge–discharge curves of  $\text{Fe}_3\text{O}_4/\text{VO}_x/\text{G-P}$  NWs at the current density of  $100 \text{ mA g}^{-1}$ ; (c) cycle performance of  $\text{Fe}_3\text{O}_4/\text{VO}_x/\text{G-P}$  NWs,  $\text{FVO@G}$  NWs and  $\text{Fe}_3\text{O}_4/\text{VO}_x\text{-P}$  NWs at the low current density of  $100 \text{ mA g}^{-1}$ ; (d) rate performance of  $\text{Fe}_3\text{O}_4/\text{VO}_x/\text{G-P}$  NWs,  $\text{FVO@G}$  NWs, and  $\text{Fe}_3\text{O}_4/\text{VO}_x\text{-P}$  NWs anodes; (e) cycling stability of  $\text{Fe}_3\text{O}_4/\text{VO}_x/\text{G-P}$  NWs at the high current density of  $2 \text{ A g}^{-1}$ ; (f) Nyquist plots of the  $\text{Fe}_3\text{O}_4/\text{VO}_x/\text{G-P}$  NWs,  $\text{FVO@G}$  NWs, and  $\text{Fe}_3\text{O}_4/\text{VO}_x\text{-P}$  NWs anodes, inset is the equivalent circuit.

Information Figure S4) reveal that the vanadium oxide is amorphous and the iron oxide is single crystalline, which are consistent with the XRD results. In addition, crystalline  $\text{Fe}_3\text{O}_4$  and amorphous vanadium oxide nanoparticles can also be observed in the TEM images of  $\text{Fe}_3\text{O}_4/\text{VO}_x\text{-P}$  NWs (Supporting Information Figure S5). Nitrogen adsorption–desorption isotherms are further measured to characterize the porous structure of the products. The Brunauer–Emmett–Teller (BET) surface area of  $\text{Fe}_3\text{O}_4/\text{VO}_x/\text{G-P}$  NWs is  $35.9 \text{ m}^2 \text{ g}^{-1}$ , which is larger than that of  $\text{FVO@G}$  NWs ( $25.0 \text{ m}^2 \text{ g}^{-1}$ ) (Supporting Information Figure S6). The nitrogen adsorption–desorption isotherms of  $\text{Fe}_3\text{O}_4/\text{VO}_x/\text{G-P}$  NWs (Figure 3a) appear to be type IV curves with the H3 hysteresis loops that can be linked to slit-shaped pores. The Barrett–Joyner–Halenda (BJH) pore-size distribution curve (inset of Figure 3a) displays the pore sizes in  $\text{Fe}_3\text{O}_4/\text{VO}_x/\text{G-P}$  NWs are in the area distribution of  $2\text{--}5 \text{ nm}$  and  $20\text{--}40 \text{ nm}$ . Raman spectra of graphene oxide precursor and  $\text{Fe}_3\text{O}_4/\text{VO}_x/\text{G-P}$  NWs are shown in Figure 2b. The bands in the range of  $1200\text{--}1460 \text{ cm}^{-1}$  and  $1510\text{--}1650 \text{ cm}^{-1}$  are attributed to the D-band ( $K$ -point phonons of  $A_{1g}$  symmetry) and G-band ( $E_{2g}$  phonons of  $C \text{ sp}^2$  atoms) of graphene,<sup>38</sup> respectively. This result indicates the existence of graphene oxide in the composite.

To determine the chemical composition of  $\text{Fe}_3\text{O}_4/\text{VO}_x/\text{G-P}$  NWs, X-ray photoelectron spectroscopy (XPS) measurements were carried out on the  $\text{FVO@G}$  NWs and  $\text{Fe}_3\text{O}_4/\text{VO}_x/\text{G-P}$  NWs to investigate the oxidation states of the vanadium and iron. Two separate peaks located at the binding energies of  $711.49$  and  $725.27 \text{ eV}$  are attributed to  $\text{Fe}^{3+} 2p_{3/2}$  and  $2p_{1/2}$  (Figure 3c). Meanwhile, a strong satellite peak that appeared at around  $719 \text{ eV}$  can be ascribed to a typical character of  $\text{Fe}^{3+}$ . The core peak for  $\text{V} 2p_{3/2}$  ( $516.80 \text{ eV}$ ) in Figure 3d can be indexed to  $\text{V}^{5+}$ . These values of binding energies are consistent with the previously reported results.<sup>39,40</sup> Therefore, the

elements of Fe and V in the as-synthesized  $\text{FVO@G}$  NWs exist as  $\text{Fe}^{3+}$  and  $\text{V}^{5+}$ , respectively. However, for the XPS spectrum of the  $\text{Fe}_3\text{O}_4/\text{VO}_x/\text{G-P}$  NWs (Figure 3e), the peaks for  $\text{Fe} 2p_{3/2}$  and  $\text{Fe} 2p_{1/2}$  can be deconvoluted into two components. Besides the existence of  $\text{Fe}^{3+}$ , two strong doublet peaks of  $\text{Fe} 2p$  appear at the binding energies of  $709.59 \text{ eV}$  ( $\text{Fe} 2p_{3/2}$ ) and  $722.80 \text{ eV}$  ( $\text{Fe} 2p_{1/2}$ ), which are attributed to  $\text{Fe}^{2+}$ . Moreover, a satellite peak at  $714.78 \text{ eV}$  is observed, which can be ascribed to a character of  $\text{Fe}^{2+}$ .<sup>41,42</sup> The  $\text{V} 2p_{3/2}$  core peak spectra for  $\text{Fe}_3\text{O}_4/\text{VO}_x/\text{G-P}$  NWs in Figure 3f is composed of two components located at  $516.80$  and  $515.60 \text{ eV}$ , respectively, which can be associated with two formal oxidation degrees,  $+5$  and  $+4$ .<sup>40</sup>

The electrochemical performances of  $\text{Fe}_3\text{O}_4/\text{VO}_x/\text{G-P}$  NWs were investigated using half cells versus  $\text{Li}/\text{Li}^+$ .<sup>43</sup> Figure 4a shows the cyclic voltammetry (CV) curves of  $\text{Fe}_3\text{O}_4/\text{VO}_x/\text{G-P}$  NWs composite electrode between  $0$  and  $3.0 \text{ V}$  at a scan rate of  $0.1 \text{ mV s}^{-1}$ . In agreement with literature,<sup>44–47</sup> it is clear that the CV curve of the first cycle is quite different from those of subsequent cycles, especially for the discharge branches. In the first discharge cycle, two well-defined peaks are observed at  $0.2$  and  $0.4 \text{ V}$ , which is usually ascribed to the occurrence of side reactions on the electrode surfaces and interfaces due to SEI formation. In comparison, the two distinct peaks are observed at about  $0.76$  and  $0.48 \text{ V}$  during discharge from the second cycle onward, corresponding to the reaction  $\text{Fe}_3\text{O}_4 + 8\text{Li}^+ + 8\text{e}^- \rightarrow 3\text{Fe}^0 + 4\text{Li}_2\text{O}$ .<sup>38</sup> Moreover, the CV curves of  $\text{Fe}_3\text{O}_4/\text{VO}_x/\text{G-P}$  NWs in the subsequent two cycles almost overlap, revealing a good reversibility. The galvanostatic charge–discharge curves of  $\text{Fe}_3\text{O}_4/\text{VO}_x/\text{G-P}$  NWs (Figure 4b) are obtained at a current density of  $100 \text{ mA g}^{-1}$  in a potential window of  $0\text{--}3.0 \text{ V}$ . In the first discharge curve, a potential plateau at about  $0.76 \text{ V}$  versus  $\text{Li}/\text{Li}^+$  is observed for  $\text{Fe}_3\text{O}_4/\text{VO}_x/\text{G-P}$  NWs, which is in a good agreement with the CV

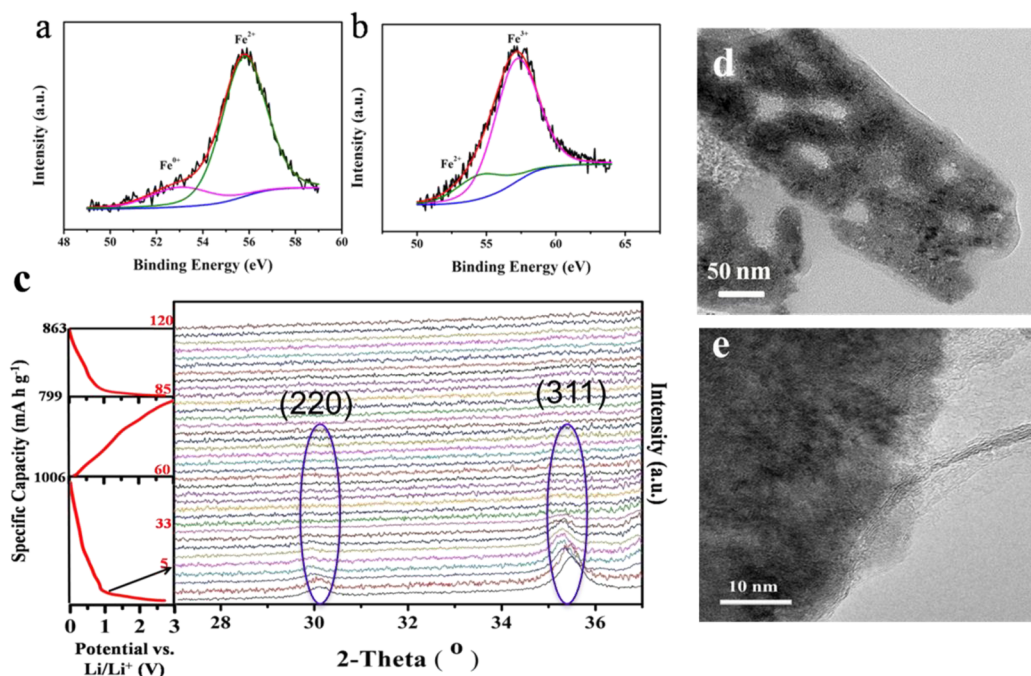


**Figure 5.** Fe 2p XPS spectra of as-prepared  $\text{Fe}_3\text{O}_4/\text{VO}_x/\text{G-P}$  NWs anode, when the cell is fully discharged to 0 V (a) and fully charged to 3 V (b); (c) in situ XRD patterns of  $\text{Fe}_3\text{O}_4/\text{VO}_x/\text{G-P}$  NWs; (d,e) TEM images of  $\text{Fe}_3\text{O}_4/\text{VO}_x/\text{G-P}$  NWs after first discharge.

results. The irreversible capacity loss in the first cycle can be attributed to the formation of SEI film.<sup>48–50</sup> Noticeably, the Coulombic efficiency of  $\text{Fe}_3\text{O}_4/\text{VO}_x/\text{G-P}$  NWs in the first cycle reaches up to 79%, much higher than other reported materials based on conversion reaction.<sup>51</sup> In addition, CV and charge–discharge curves of FVO@G NWs are also carried out as control experiments (Supporting Information Figure S7 and S8). After 30 cycles, the  $\text{Fe}_3\text{O}_4/\text{VO}_x/\text{G-P}$  NWs composite electrode exhibits a reversible capacity of about  $1164 \text{ mA h g}^{-1}$ . Figure 4c shows cycle performance of the  $\text{Fe}_3\text{O}_4/\text{VO}_x/\text{G-P}$  NWs, FVO@G NWs and  $\text{Fe}_3\text{O}_4/\text{VO}_x\text{-P}$  NWs at a current density of  $100 \text{ mA g}^{-1}$  for 30 cycles. It is obvious that  $\text{Fe}_3\text{O}_4/\text{VO}_x/\text{G-P}$  NWs exhibits highest reversible capacity after 30 cycles. To further investigate the electrochemical performance of  $\text{Fe}_3\text{O}_4/\text{VO}_x/\text{G-P}$  NWs, FVO@G NWs, and  $\text{Fe}_3\text{O}_4/\text{VO}_x\text{-P}$  NWs the rate capability of the three samples were further compared. With the rate increasing, the  $\text{Fe}_3\text{O}_4/\text{VO}_x/\text{G-P}$  NWs anode exhibits the least capacity decrease among the three samples (Figure 4d and Supporting Information Figure S10). For example, when the current density increases to  $2 \text{ A g}^{-1}$ , the specific capacity of  $\text{Fe}_3\text{O}_4/\text{VO}_x/\text{G-P}$  NWs still remains  $808 \text{ mA h g}^{-1}$  (84.4% of the capacity obtain in  $0.1 \text{ A g}^{-1}$ ), which is much larger than that of FVO@G NWs (12.0%) and  $\text{Fe}_3\text{O}_4/\text{VO}_x\text{-P}$  NWs (11.7%). Remarkably, the reversible capacity is also retained to about  $500 \text{ mA h g}^{-1}$  even with the rate up to  $5 \text{ A g}^{-1}$  (Supporting Information Figure S11). Additionally, the  $\text{Fe}_3\text{O}_4/\text{VO}_x/\text{G-P}$  NWs anode also exhibits good cycling stability at high current density as shown in Figure 4e. The capacity retention remains 99% after 100 cycles at  $2 \text{ A g}^{-1}$  (capacity retention = final specific capacity/the highest specific capacity during cycling). The cycling performance of  $\text{Fe}_3\text{O}_4/\text{VO}_x/\text{G-P}$  NWs, FVO@G, and  $\text{Fe}_3\text{O}_4/\text{VO}_x\text{-P}$  NWs at  $2 \text{ A g}^{-1}$  for 200 cycles is also shown in Supporting Information Figure S10. Such excellent high rate performance and cycling stability at high charge/discharge rates are significantly higher than in previously reported works on  $\text{Fe}_3\text{O}_4$  nanostructures and

$\text{Fe}_3\text{O}_4/\text{carbon}$  hybrids (as shown in Supporting Information Figure S12). Moreover, three-electrode cell was assembled to test the galvanostatic charge and discharge curves of  $\text{Fe}_3\text{O}_4/\text{VO}_x/\text{G-P}$  NWs in voltage ranges in 0–3.0 and 0.1–3.0 V (vs  $\text{Li}/\text{Li}^+$ ) at  $2 \text{ A g}^{-1}$  (Supporting Information Figure S13), the discharge capacity of  $\text{Fe}_3\text{O}_4/\text{VO}_x/\text{G-P}$  NWs in voltage ranges in 0–3.0 and 0.1–3.0 V displayed almost the same (Supporting Information Figure S14), indicating that the metallic Li deposition on the electrode might have little contribution to the capacity when the cutoff voltage is set to 0 V versus  $\text{Li}/\text{Li}^+$ .

The electrochemical impedance spectra (EIS) were used to provide further insights (Figure 4f). All the Nyquist plots are composed of a depressed semicircle in the medium-frequency region followed by a slanted line in the low-frequency region. Figure 4f inset shows the equivalent circuit that gives rise to a good fit for the EIS spectra of  $\text{Fe}_3\text{O}_4/\text{VO}_x/\text{G-P}$  NWs,  $\text{Fe}_3\text{O}_4/\text{VO}_x\text{-P}$  NWs and FVO@G NWs with the fitting parameters presented in Supporting Information Table S2. In the equivalent circuit (inset of Figure 4f),  $R_s$  represents the equivalent series resistance that includes all Ohmic resistance due to the electrolyte and other parts of the cell. CPE refers to constant phase elements, revealing the nonideal capacitance due to the surface roughness, while  $R_{ct}$  and  $R_f$  stand for the charge transfer resistance through the electrode/electrolyte interface and the contacts in between nanowires, respectively.<sup>52</sup> The values of  $R_{ct}$  for the  $\text{Fe}_3\text{O}_4/\text{VO}_x/\text{G-P}$  NWs electrodes were calculated to be  $56 \Omega$ , which is much lower than that of  $\text{Fe}_3\text{O}_4/\text{VO}_x\text{-P}$  NWs ( $146 \Omega$ ) and FVO@G NWs ( $112 \Omega$ ), respectively. This indicates the unique hierarchical porous nanowires indeed enhance the charge transfer across the electrode/electrolyte interface.

XPS was used to elucidate the valence states change of the element (Fe) in sample  $\text{Fe}_3\text{O}_4/\text{VO}_x/\text{G-P}$  NWs during charge/discharge process (Figure 5a,b). The broad peak for Fe in the discharged sample can be deconvoluted into two peaks of  $3p$  at 53.2 and 56 eV corresponding to  $\text{Fe}^0$  and  $\text{Fe}^{2+}$  states,

respectively. When the cell is fully charged, the broad peak for Fe in the charged sample can be deconvoluted into two peaks of 3p at 54.9 and 57.7 eV corresponding to Fe<sup>2+</sup> and Fe<sup>3+</sup> states, respectively. These values of binding energies are consistent with the previously reported results.<sup>53,54</sup> To further investigate the reaction mechanisms that occur in Fe<sub>3</sub>O<sub>4</sub>/VO<sub>x</sub>/G-P NWs electrode materials, we used an in situ X-ray diffraction technique. The as-prepared composites in situ cell was discharged to 0 V and then charged to 3.0 V using a constant current of 100 mA g<sup>-1</sup> at 25 °C and was never removed from the diffractometer (Figure 5c). During the first discharge the diffraction peaks (30.1° and 35.5°, which are in agreement with those of the (220) and (311) planes of Fe<sub>3</sub>O<sub>4</sub>, respectively) from the Fe<sub>3</sub>O<sub>4</sub>/VO<sub>x</sub>/G-P NWs shift to a lower angle due to the expansion of the electrode host matrix as Li atoms are inserted. In addition, the two diffraction peaks become weaker and weaker until fully disappeared, and no obvious diffraction peak can be observed during the following charge and discharge. This is likely due to the amorphous electrode materials formed after Li<sup>+</sup> insertion. To further investigate the phase transformation details of the sample, we carried out the TEM analysis of Fe<sub>3</sub>O<sub>4</sub>/VO<sub>x</sub>/G-P NWs electrode material after cycle. The TEM images (Figure 5d,e) show the amorphous material can be observed clearly (crystalline Fe<sub>3</sub>O<sub>4</sub> is difficult to find in Fe<sub>3</sub>O<sub>4</sub>/VO<sub>x</sub>/G-P NWs).

On the basis of the results above, the superior high-rate and cycling performance of Fe<sub>3</sub>O<sub>4</sub>/VO<sub>x</sub>/G-P NWs are attributed to the synergetic advantages of graphene and porous nanowires, as illustrated in Figure 1. On the one hand, conductive graphene-decorated porous nanowire offers efficient electron transport and rapid ion diffusion pathways, provide mechanical flexibility for the iron oxide to accommodate volume changes during cycling. On the other hand, the porous structure increases the contact area between electrode and electrolyte, which reduce the R<sub>ct</sub> (Figure 4f), resulting in the excellent rate capability. Besides, the porous nanowires reduce the self-aggregation of active materials and the amorphous vanadium oxides matrixes supporting stable porous structure can also rapidly accommodate the volume variations during repeated Li<sup>+</sup> insertion/extraction, which guarantee the effective electron contact upon longed cycling, leading to the attractive structural stability (Supporting Information Figure S15) and good cycle life.

In summary, amorphous vanadium oxides matrixes supporting hierarchical porous Fe<sub>3</sub>O<sub>4</sub>/graphene nanowires have been synthesized via a facile phase separation process in H<sub>2</sub>/Ar. Fe<sub>3</sub>O<sub>4</sub>/VO<sub>x</sub>/G-P NWs exhibit high reversible capacity (1146 mAh g<sup>-1</sup>), remarkable rate capability (5 A g<sup>-1</sup>), and good high-rate cycling stability (the capacity retention remains 99% after 100 charge/discharge cycles at 2 A g<sup>-1</sup>). Moreover, the electrochemical reaction mechanism of the Fe<sub>3</sub>O<sub>4</sub>/VO<sub>x</sub>/G-P NWs was also investigated by in situ XRD and XPS. The amorphization and conversion reactions between Fe and Fe<sub>3</sub>O<sub>4</sub> are revealed proceeding on the amorphous vanadium oxide matrixes. The excellent electrochemical performance can be attributed to the synergetic advantages of graphene and porous nanowires, which provide bicontinuous electron/ion pathways, large electrode–electrolyte contact area and facile strain relaxation. This kind of novel porous composite nanowire structure and the effective strategy can be further applied to the high-performance energy storage devices.

## ■ ASSOCIATED CONTENT

### Supporting Information

Additional information and figures. This material is available free of charge via the Internet at <http://pubs.acs.org>.

## ■ AUTHOR INFORMATION

### Corresponding Authors

\*E-mail: (C.H.) [hch5927@whut.edu.cn](mailto:hch5927@whut.edu.cn).

\*E-mail: (L.M.) [mlq518@whut.edu.cn](mailto:mlq518@whut.edu.cn).

### Author Contributions

<sup>§</sup>These authors contributed equally to this work.

### Notes

The authors declare no competing financial interest.

## ■ ACKNOWLEDGMENTS

This work was supporting by the National Basic Research Program of China (2013CB934103, 2012CB933003), The National Science Fund for Distinguished Young Scholarthe National Natural Science Foundation of China (51272197, 51302203), the International Science and Technology Cooperation Program of China (2013DFA50840), the Hubei Science Fund for Distinguished Young Scholars (2014CFA035), the Fundamental Research Funds for the Central Universities (2014-YB-001, 2014-YB-002, 2014-ZY-016, 2013-ZD-7, 2014-VII-007), and the Students Innovation and Entrepreneurship Training Program (20131049701008). Thanks to Professor C. M. Lieber of Harvard University and Professor D. Y. Zhao of Fudan University for strong support and stimulating discussion.

## ■ REFERENCES

- (1) Liu, C.; Li, F.; Ma, L. P.; Cheng, H. M. *Adv. Mater.* **2010**, *22*, E28–E62.
- (2) Xiao, J.; Wan, L.; Yang, S.; Xiao, F.; Wang, S. *Nano Lett.* **2014**, *14*, 831–838.
- (3) Liu, H.; Yang, W. *Energy Environ. Sci.* **2011**, *4*, 4000–4008.
- (4) Kang, B.; Ceder, G. *Nature* **2009**, *458*, 190–193.
- (5) Tarascon, J. M.; Armand, M. *Nature* **2001**, *414*, 359–367.
- (6) Wang, S.; Li, S.; Sun, Y.; Feng, X.; Chen, C. *Energy Environ. Sci.* **2011**, *4*, 2854–2857.
- (7) Li, W.; Dahn, J.; Wainwright, D. *Science* **1994**, *264*, 1115–1118.
- (8) Cui, Z. M.; Jiang, L. Y.; Song, W. G.; Guo, Y. G. *Chem. Mater.* **2009**, *21*, 1162–1166.
- (9) Taberna, P. L.; Mitra, S.; Poizot, P.; Simon, P.; Tarascon, J. M. *Nat. Mater.* **2006**, *5*, 567–573.
- (10) Wang, Y.; Cao, G. *Adv. Mater.* **2008**, *20*, 2251–2269.
- (11) Mai, L.; Dong, F.; Xu, X.; Luo, Y.; An, Q.; Zhao, Y.; Pan, J.; Yang, J. *Nano Lett.* **2013**, *13*, 740–745.
- (12) Wang, Y.; Wang, Y.; Jia, D.; Peng, Z.; Xia, Y.; Zheng, G. *Nano Lett.* **2014**, *14*, 1080–1084.
- (13) Zhang, C.; Chen, Z.; Guo, Z.; Lou, X. W. *Energy Environ. Sci.* **2013**, *6*, 974–978.
- (14) Wei, Q.; An, Q.; Chen, D.; Mai, L.; Chen, S.; Zhao, Y.; Hercule, K. M.; Xu, L.; Minhas-Khan, A.; Zhang, Q. *Nano Lett.* **2014**, *14*, 1042–1048.
- (15) Xia, Y.; Yang, P.; Sun, Y.; Wu, Y.; Mayers, B.; Gates, B.; Yin, Y.; Kim, F.; Yan, H. *Adv. Mater.* **2003**, *15*, 353–389.
- (16) Tian, B.; Zheng, X.; Kempa, T. J.; Fang, Y.; Yu, N.; Yu, G.; Huang, J.; Lieber, C. M. *Nature* **2007**, *449*, 885–889.
- (17) Xu, S.; Qin, Y.; Xu, C.; Wei, Y.; Yang, R.; Wang, Z. L. *Nat. Nanotechnol.* **2010**, *5*, 366–373.
- (18) Yan, H.; Choe, H. S.; Nam, S.; Hu, Y.; Das, S.; Klemic, J. F.; Ellenbogen, J. C.; Lieber, C. M. *Nature* **2011**, *470*, 240–244.
- (19) (a) Liu, J.; Xie, C.; Dai, X. C.; Jin, L. H.; Zhou, W.; Lieber, C. M. *Proc. Natl. Acad. Sci. U.S.A.* **2013**, *110*, 6694–6699. (b) Yang, C.; Zhao, H. B.; Hou, Y. L.; Ma, D. *J. Am. Chem. Soc.* **2012**, *134*, 15814–15821.

- (c) Qie, L.; Chen, W. M.; Xu, H. H.; Xiong, X. Q.; Jiang, Y.; Zou, F.; Hu, X. L.; Xin, Y.; Zhang, Z. L.; Huang, Y. H. *Energy Environ. Sci.* **2013**, *6*, 2497–2504. (d) Niu, C. J.; Meng, J. S.; Han, C. H.; Zhao, K. N.; Yan, M. Y.; Mai, L. Q. *Nano Lett.* **2014**, *14*, 2873–2878.
- (20) Mai, L.; An, Q.; Wei, Q.; Fei, J.; Zhang, P.; Xu, X.; Zhao, Y.; Yan, M.; Wen, W.; Xu, L. *Small* **2014**, *10*, 3032–3037.
- (21) Mai, L.; Wei, Q.; An, Q.; Tian, X.; Zhao, Y.; Xu, X.; Xu, L.; Chang, L.; Zhang, Q. *Adv. Mater.* **2013**, *25*, 2969–2973.
- (22) Arruda, T. M.; Heon, M.; Presser, V.; Hillesheim, P. C.; Dai, S.; Gogotsi, Y.; Kalinin, S. V.; Balke, N. *Energy Environ. Sci.* **2013**, *6*, 225–231.
- (23) Tsai, W.-Y.; Gao, P. C.; Daffos, B.; Taberna, P. L.; Perez, C. R.; Gogotsi, Y.; Favier, F.; Simon, P. *Electrochem. Commun.* **2013**, *34*, 109–112.
- (24) Du, X.; He, W.; Zhang, X.; Yue, Y.; Liu, H.; Zhang, X.; Min, D.; Ge, X.; Du, Y. *J. Mater. Chem.* **2012**, *22*, 5960–5969.
- (25) Shen, L.; Zhang, X.; Uchaker, E.; Yuan, C.; Cao, G. *Adv. Energy Mater.* **2012**, *2*, 691–698.
- (26) Liu, H.; Su, D.; Zhou, R.; Sun, B.; Wang, G.; Qiao, S. Z. *Adv. Energy Mater.* **2012**, *2*, 970–975.
- (27) Shi, Y.; Hua, C.; Li, B.; Fang, X.; Yao, C.; Zhang, Y.; Hu, Y. S.; Wang, Z.; Chen, L.; Zhao, D. *Adv. Funct. Mater.* **2013**, *23*, 1832–1838.
- (28) Chan, C. K.; Peng, H.; Liu, G.; McIlwrath, K.; Zhang, X. F.; Huggins, R. A.; Cui, Y. *Nat. Nanotechnol.* **2008**, *3*, 31–35.
- (29) Ding, R.; Liu, J.; Jiang, J.; Wu, F.; Zhu, J.; Huang, X. *Catal. Sci. Technol.* **2011**, *1*, 1406–1411.
- (30) Shim, H. W.; Lee, D. K.; Cho, I.-S.; Hong, K. S.; Kim, D. W. *Nanotechnol.* **2010**, *21*, 255706.
- (31) Yang, Y.; Wang, C.; Yue, B.; Gambhir, S.; Too, C. O.; Wallace, G. G. *Adv. Energy Mater.* **2012**, *2*, 266–272.
- (32) Han, C.; Yan, M.; Mai, L.; Tian, X.; Xu, L.; Xu, X.; An, Q.; Zhao, Y.; Ma, X.; Xie, J. *Nano Energy* **2013**, *2*, 916–922.
- (33) Zhu, Y.; Murali, S.; Stoller, M. D.; Ganesh, K.; Cai, W.; Ferreira, P. J.; Pirkle, A.; Wallace, R. M.; Cychosz, K. A.; Thommes, M. *Science* **2011**, *332*, 1537–1541.
- (34) Lin, J.; Raji, A. R. O.; Nan, K.; Peng, Z.; Yan, Z.; Samuel, E. L.; Natelson, D.; Tour, J. M. *Adv. Funct. Mater.* **2014**, *24*, 2044–2048.
- (35) Materials synthesis: In a typical synthesis,  $\text{FeCl}_3 \cdot 6\text{H}_2\text{O}$  (2 mmol, Sinopharm Chemical Reagent Co., Ltd.) was first dissolved in 10 mL water under stirring, followed by the addition of 20 mL graphene oxide ( $2 \text{ g L}^{-1}$ ) aqueous dispersion. The graphene oxide precursor was “graphene oxide dispersion liquid” chemical pure and purchased from XianFeng Nano Inc. (Nanjing, China).  $\text{NH}_4\text{VO}_3$  powder (2 mmol, Sinopharm Chemical Reagent Co., Ltd.) was then dissolved in 10 mL water under stirring at  $80^\circ\text{C}$ , thereafter, the  $\text{NH}_4\text{VO}_3$  solution was slowly added into the  $\text{FeCl}_3$  and graphene oxide mixture under stirring. After 10 min, the suspension was transferred into a 50 mL Teflon-lined stainless steel autoclave. The autoclave was heated at  $180^\circ\text{C}$  for 3 h and then cooled to room temperature naturally. The precipitate (FVO@G NWs) was collected by centrifugation and washed three times with water and ethanol respectively and dried under vacuum at  $70^\circ\text{C}$  for 12 h. Finally, the amorphous vanadium oxides matrixes supporting hierarchical porous  $\text{Fe}_3\text{O}_4$ /graphene nanowires ( $\text{Fe}_3\text{O}_4/\text{VO}_x/\text{G-P}$  NWs) were obtained by annealing the precipitate at  $500^\circ\text{C}$  for 4 h in  $\text{H}_2/\text{Ar}$  (5%:95%) with a heating rate of  $5^\circ\text{C min}^{-1}$ . In addition, bare  $\text{Fe}_3\text{O}_4/\text{VO}_x\text{-P}$  NWs was synthesized in the same procedure without the addition of graphene oxide. Characterization: X-ray diffraction (XRD) measurements were performed to investigate the crystallographic information using a D8 Advance X-ray diffractometer with nonmonochromated  $\text{Cu K}\alpha$  X-ray source. Scanning electron microscopy (SEM) images were collected with a JEOL-7100F microscopy at an acceleration voltage of 15 kV. Transmission electron microscopy (TEM) images and high-resolution transmission electron microscopy (HRTEM) images were recorded by using a JEM-2100F STEM/EDS microscope. Brunauer–Emmett–Teller (BET) surface areas were measured using Tristar II 3020 instrument to measure the adsorption of nitrogen. Raman spectra were obtained using a Renishaw INVIA micro-Raman spectroscopy system. X-ray photoelectron spectroscopy (XPS) measurements were obtained using a VG MultiLab 2000 instrument. The mass ratio of Fe/V in the samples were characterized by inductively coupled plasma (ICP) test using PerkinElmer Optima 4300DV spectrometer.
- (36) Kaneti, Y. V.; Zhang, Z.; Yue, J.; Jiang, X.; Yu, A. J. *Nanopart. Res.* **2013**, *15*, 1–15.
- (37) Chen, J.; Xu, L. N.; Li, W. Y.; Gou, X. I. *Adv. Mater.* **2005**, *17*, 582–586.
- (38) Shi, Y.; Wang, J. Z.; Chou, S. L.; Wexler, D.; Li, H. J.; Ozawa, K.; Liu, H. K.; Wu, Y. P. *Nano Lett.* **2013**, *13*, 4715–4720.
- (39) Sim, D. H.; Rui, X.; Chen, J.; Tan, H.; Lim, T. M.; Yazami, R.; Hng, H. H.; Yan, Q. *RSC Adv.* **2012**, *2*, 3630–3633.
- (40) Hopfengärtner, G.; Borgmann, D.; Rademacher, I.; Wedler, G.; Hums, E.; Spitznagel, G. W. *J. Electron Spectrosc.* **1993**, *63*, 91–116.
- (41) Yamashita, T.; Hayes, P. *Appl. Surf. Sci.* **2008**, *254*, 2441–2449.
- (42) Bhargava, G.; Gouzman, I.; Chun, C.; Ramanarayanan, T.; Bernasek, S. *Appl. Surf. Sci.* **2007**, *253*, 4322–4329.
- (43) Electrochemical measurements: The electrochemical properties were evaluated by assembly of 2016 coin cells in a glovebox filled with pure argon gas. The working electrode was prepared by mixing the as-synthesized materials, acetylene black, and carboxyl methyl cellulose (CMC) at a weight ratio of 70:20:10. The slurry was casted onto Cu foil and dried under a vacuum oven at  $150^\circ\text{C}$  for 2 h. The loading of active materials was  $1.2\text{--}1.5 \text{ mg cm}^{-2}$ . Lithium pellets were used as the anode. The electrolyte was composed of 1 M LiPF<sub>6</sub> dissolved in ethylene carbonate (EC)/dimethyl carbonate (DMC) with a volume ratio of 1:1. Galvanostatic charge/discharge cycling was studied in a potential range of 0–3.0 V versus  $\text{Li/Li}^+$  with a multichannel battery testing system (LAND CT2001A). Cyclic voltammetry (CV) and AC-impedance spectra were tested with an electrochemical workstation (Autolab PGSTAT 302N). Three-electrode cell fabrication and electrochemical measurement: the working electrode and the electrolyte solution was prepared the same as that of 2016 coin cells, two pieces of Li metals worked as the counter and reference electrode, respectively. Galvanostatic charge/discharge cycling was tested in a potential range of 0–3.0 and 0.1–3.0 V versus  $\text{Li/Li}^+$  with CHI605e.
- (44) Wang, Y.; Zhang, L.; Gao, X. H.; Mao, L.; Hu, Y.; Lou, X. W. D. *Small* **2014**, DOI: 10.1002/smll.201400239.
- (45) Yang, Z.; Shen, J.; Archer, L. A. *J. Mater. Chem.* **2011**, *21*, 11092–11097.
- (46) Piao, Y.; Kim, H. S.; Sung, Y. E.; Hyeon, T. *Chem. Commun.* **2010**, *46*, 118–120.
- (47) He, C.; Wu, S.; Zhao, N.; Shi, C.; Liu, E.; Li, J. *ACS Nano* **2013**, *7*, 4459–4469.
- (48) Liu, H.; Wang, G.; Wang, J.; Wexler, D. *Electrochem. Commun.* **2008**, *10*, 1879–1882.
- (49) Muraliganth, T.; Murugan, A. V.; Manthiram, A. *Chem. Commun.* **2009**, *47*, 7360–7362.
- (50) Wang, J. Z.; Zhong, C.; Wexler, D.; Idris, N. H.; Wang, Z. X.; Chen, L. Q.; Liu, H. K. *Chem.—Eur. J.* **2011**, *17*, 661–667.
- (51) Yang, G.; Cui, H.; Yang, G.; Yang, G. W.; Wang, C. X. *ACS Nano* **2014**, *8*, 4474–4487.
- (52) Raju, V.; Rains, J.; Gates, C.; Luo, W.; Wang, X.; Stickle, W. F.; Stucky, G. D.; Ji, X. *Nano Lett.* **2014**, *14*, 4119–4124.
- (53) Joyner, D. J.; Johnson, O.; Hercules, D. M. *J. Am. Chem. Soc.* **1980**, *102*, 1910–1917.
- (54) De Donato, Ph.; Mustin, C.; Benoit, R.; Erre, R. *Appl. Surf. Sci.* **1993**, *68*, 81–93.